THERMOELECTRICS

Quadruple-band synglisis enables high thermoelectric efficiency in earth-abundant tin sulfide crystals

Shan Liu[1,2], Shulin Bai[2], Yi Wen[2,3], Jing Lou[4], Yongzhen Jiang[5], Yingcai Zhu[2,6], Dongrui Liu[2], Yichen Li[2], Haonan Shi[2], Shibo Liu[2], Lei Wang[2], Junqing Zheng[2], Zhe Zhao[2], Yongxin Qin[2,6], ZhongKai Liu[5], Xiang Gao[7], Bingchao Qin[1,2]*, Cheng Chang[1,2]*, Chao Chang[4,8]*, Li-Dong Zhao[1,2,3]*

Thermoelectrics have been limited by the scarcity of their constituent elements, especially telluride. The earth-abundant, wide-bandgap ($E_g \approx 46\ k_B T$) tin sulfide (SnS) has shown promising performance in its crystal form. We improved the thermoelectric efficiency in SnS crystals by promoting the convergence of energy and momentum of four valence bands, termed quadruple-band synglisis. We introduced more Sn vacancies to activate quadruple-band synglisis and facilitate carrier transport by inducing SnS_2 in selenium (Se)–alloyed SnS, leading to a high dimensionless figure of merit (ZT) of ~1.0 at 300 kelvin and an average ZT of ~1.3 at 300 to 773 kelvin in p-type SnS crystals. We further obtained an experimental efficiency of ~6.5%, and our fabricated cooler demonstrated a maximum cooling temperature difference of ~48.4 kelvin at 353 kelvin. Our observations should draw interest to earth-abundant SnS crystals for applications of waste-heat recovery and thermoelectric cooling.

Thermoelectric technology offers an alternative solution for the emerging demand of low-carbon and clean-energy technologies by enabling energy generation or fast cooling through the direct conversion between heat and electricity (1, 2). The key challenge in advancing thermoelectric technology lies in achieving high energy-conversion efficiency, which is predominantly influenced by the properties of thermoelectric materials, as expressed by the dimensionless figure of merit (ZT) with $ZT = (S^2\sigma T)/\kappa_{tot}$, where S is the Seebeck coefficient, σ is the electrical conductivity, T is the absolute temperature, and κ_{tot} is the total thermal conductivity (3, 4). The inherent conflicts between thermal and electrical transport pose a considerable challenge to enhancing the overall ZT (3). To decouple the complex transport, researchers have proposed various optimization strategies, including carrier concentration and mobility optimization (5), band structure engineering (6, 7), all-scale defects engineering (8, 9), and lattice plainification (5, 10, 11), and so on. Consequently, substantial improvements of ZT values have been achieved in various thermoelectric systems, such as Bi_2Te_3 (12, 13),

Pb(S, Se, Te) (14, 15), Sn(S, Se, Te) (16–18), Cu_2(S, Se, Te) (19, 20), GeTe (21, 22), Mg_3(Bi, Sb)$_2$ (23, 24), and so on.

The concern over rare and toxic elements in advanced thermoelectric materials such as Bi_2Te_3 and PbTe has shifted some of the research interest toward developing high-performance thermoelectric materials that use earth-abundant, low-cost, and nontoxic elements. SnSe has been developed as one important thermoelectric material that aligns with these objectives (25, 26). Both p-type and n-type SnSe exhibit excellent thermoelectric performance (27, 28), which originates from the strong anharmonicity (29), multiband structures (30), and distinctive three-dimensional charge and two-dimensional phonon transport characteristics (31). SnS, an analog of SnSe, exhibits even higher earth abundance and lower cost, making it a promising candidate for constructing high-efficiency thermoelectric modules (32, 33). In particular, the raw material reserves of Sn and S are considerably more abundant than those of other common constituent elements in thermoelectric materials (fig. S1). In addition, PbS-based (34–37), Cu_2S-based (38–41), Cu-Sn-S–based (42–44), and Cu-Fe-S–based (45, 46) sulfide compounds have also been well developed. Initially, SnS exhibited extremely inferior thermoelectric performance in its polycrystalline form owing to its poor electrical properties, and the large bandgap (~1.2 eV; 46 $k_B T$, where k_B is the Boltzmann constant and T is temperature) makes it difficult to dope with a proper carrier concentration (32, 33, 47). Single-crystal growth provides an effective approach to enhance the electrical performance because of the high in-plane carrier mobility. Subsequently, substantial advances have been made, especially in p-type SnS crystals, by effective hole doping and the enhanced inter-

play between multiple valence bands, further elucidating the promising potential of SnS (17, 48, 49).

The complex electronic band structure plays an important role in achieving excellent thermoelectric properties in SnS (17, 49). There are multiple valence band maxima (VBM) with small energy offset (ΔE) in SnS. To simplify the discussion, we designated valence bands 1 to 4 based on the energy level, with their respective maxima denoted as VBM1 to VBM4 (Fig. 1A). Specifically, ΔE between VBM1 and VBM3 of SnS is ~0.13 eV, and heavy hole doping activates the three valence bands for electrical transport, along with the promoted band convergence between them. The triple-band convergence substantially decouples the effective mass and carrier mobility, leading to a high ZT of ~1.6 at 873 K in p-type SnS crystals (17). Similarly, this triple-band synglisis contributes to the promoted ZT values in SnSe (27). To further enhance the thermoelectric performance of SnS, it might be essential to activate more bands and use their synglisis to enhance the carrier transport. However, this remains a challenge, and no experimental attempts have been made toward activating four bands yet.

In this work, we successfully activated four valence bands and realized the quadruple-band synglisis in the earth-abundant SnS crystals, which substantially enhanced the thermoelectric efficiency in terms of power generation as well as thermoelectric cooling. We realized this by introducing SnS_2 in SnS to create more Sn vacancies, which facilitates an ultrahigh hole carrier concentration to lower the Fermi level and activate four valence bands while enabling Sn vacancies in SnS to also effectively engineer the valence bands to realize the quadruple-band synglisis, a combination of triple-band convergence and triple-band synglisis. We first refined the composition of p-type Se-alloyed SnS crystal, 2% Na–doped $SnS_{1-y}Se_y$. Because 2% Na doping is fixed in all samples, we have abbreviated the sample names by omitting Na throughout the text. We obtained an optimized matrix of $SnS_{0.9}Se_{0.1}$ crystal. We then introduced SnS_2 into the $SnS_{0.9}Se_{0.1}$ matrix and obtained $SnS_{0.9}Se_{0.1}$ with more Sn vacancies, which we labeled as $SnS_{0.9}Se_{0.1}+xSnS_2$ (where x = 0, 0.01, 0.02, 0.03, and 0.04). With the increasing fraction of SnS_2, the Hall carrier concentration (n_H) increased from ~2.7×10^{19} to ~$4.9 \times 10^{19}\ cm^{-3}$, which we confirmed with terahertz (THz) spectroscopy measurements. The hole carrier concentration that was nearly doubled contributes substantially to the participation of four valence bands in the carrier transport, which leads to the optimized electrical properties. We characterized the temperature-dependent band structures of $SnS_{0.9}Se_{0.1}+0.03SnS_2$ by using high-temperature synchrotron radiation x-ray diffraction (SR-XRD), angle-resolved photoemission spectroscopy (ARPES), and density

[1]Center for Bioinspired Science and Technology, Hangzhou International Innovation Institute, Beihang University, Hangzhou, China. [2]School of Materials Science and Engineering, Beihang University, Beijing, China. [3]Tianmushan Laboratory, Yuhang District, Hangzhou, China. [4]Innovation Laboratory of Terahertz Biophysics, National Innovation Institute of Defense Technology, Beijing, China. [5]School of Physical Science and Technology, ShanghaiTech Laboratory for Topological Physics, ShanghaiTech University, Shanghai, China. [6]Institute of Atomic Manufacturing, Beihang University, Beijing, China. [7]Center for High Pressure Science and Technology Advanced Research (HPSTAR), Beijing, China. [8]School of Physics, Peking University, Beijing, China.
*Corresponding author. Email: qinbingchao@buaa.edu.cn (B.Q.); changchengcc@buaa.edu.cn (Che.C.); gwyzlzssb@pku.edu.cn (Cha.C.); zhaolidong@buaa.edu.cn (L.-D.Z.)

functional theory (DFT) calculations. Our results elucidated that, in addition to the interplay between VBM1, VBM2, and VBM3 (*17*), VBM4 gradually increases and leads to a lower ΔE between VBM1 and VBM4 after introducing SnS_2, and the pudding-mold VBM1 and VBM4 gradually merge with rising temperature, ultimately forming the quadruple-band synglisis (Fig. 1A). The quadruple-band synglisis facilitates the electrical performance, especially by enlarging the effective mass m^*. Consequently, we obtained a high power factor ($PF = S^2\sigma$) of ~58 μW cm^{-1} K^{-2} at 300 K in p-type $SnS_{0.9}S_{0.1}+0.03SnS_2$ crystal, which outperforms other reported SnS-based compounds with fewer valence bands participating in carrier transport (*17, 49*) (Fig. 1B). The quadruple-band synglisis leads to a notable ZT curve over a wide temperature range (Fig. 1C). These results lay a robust foundation for earth-abundant SnS-based thermoelectric devices in both power generation and cooling applications.

Results

Optimizing the electrical transport performance of SnS crystal

We selected 2% Na as the dopant primarily to optimize n_H in all p-type SnS samples. We then prepared a series of $SnS_{1-y}Se_y$ crystals to optimize the PF. The electrical transport properties of $SnS_{1-y}Se_y$ crystals are presented in fig. S2, including σ, S, and PF. We refined the composition gradient and found that $SnS_{0.9}Se_{0.1}$ exhibits the optimal electrical transport properties, with a maximum PF reaching ~30 μW cm^{-1} K^{-2} at 300 K. Accordingly, we selected $SnS_{0.9}Se_{0.1}$ as the matrix for further investigations. We then added excess S in $SnS_{0.9}Se_{0.1}$ to promote additional Sn vacancies, which we expected would increase the hole carrier concentration and promote multiple band transport, similar to the role of excess Se in SnSe crystal (*50*). We collected x-ray diffraction (XRD) and Laue diffraction patterns (fig. S3), which confirmed that all crystal samples could be identified as the single SnS phase, adhering to the *Pnma* space group. We measured the electrical transport properties of $SnS_{0.9}Se_{0.1}+xSnS_2$ along the in-plane direction (*b* axis) (Fig. 2) and observed electrical transport performance enhancement with the addition of excess S. Specifically, room-temperature σ increases considerably from ~580 to ~1500 S cm^{-1} with an increasing amount of SnS_2 (Fig. 2A), whereas S remains as high as ~200 μV K^{-1}, even with the hole carrier concentration nearly doubled (Fig. 2B and fig. S4). The cooperative regulation of σ and S results in a high PF value of ~58 μW cm^{-1} K^{-2} in $SnS_{0.9}Se_{0.1}+0.03SnS_2$ (Fig. 2C), the highest value among the previously reported SnS-based compounds (*17, 48, 49*).

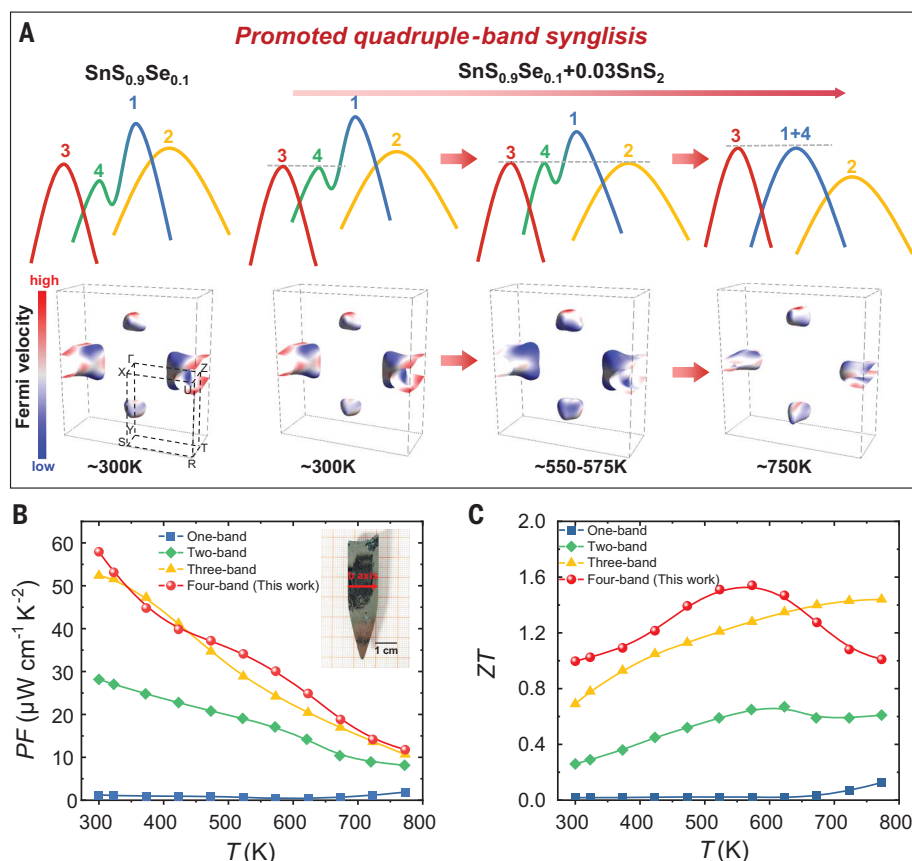To get a deep insight into the origin of the high PF, we conducted room-temperature Hall

Fig. 1. Quadruple-band synglisis and the thermoelectric performance of p-type SnS crystals with multiple bands participated in electrical transport. (**A**) Schematic of the quadruple-band synglisis and the corresponding Fermi surfaces at the indicated temperatures for $SnS_{0.9}Se_{0.1}$ and $SnS_{0.9}Se_{0.1}+0.03SnS_2$. The colored numbers and peaks indicate VBM1 to VBM4. (**B**) PF and (**C**) ZT for $SnS_{0.9}Se_{0.1}+0.03SnS_2$ crystal with four-band transport compared with PF and ZT for SnS crystals with one-, two-, and three-band transport (*17, 49*).

measurements (fig. S4). The results showed that n_H gradually increases with the rising SnS_2 fraction and reaches as high as ~4.9×10^{19} cm^{-3} at 300 K. This is likely the highest hole carrier concentration obtained so far in p-type SnS, which could be essential to lower the Fermi level and activate more valence bands to facilitate carrier transport. To reveal the important role of the electronic bands for electrical transport, we used three different band models to evaluate the effect of multiple band transport, including the two-band, three-band, and four-band models (Fig. 2, D and E). An experimentally determined S with x equal to 0.03 and 0.04 fit well with the theoretical curves of the four-band model, indicating that all four valence bands participate in the electrical transport, and the μ we measured remained higher than 150 cm^2 V^{-1} s^{-1}, which is indicative of the advantage of in-plane carrier transport in crystals with layered structures. Furthermore, the S values of $SnS_{0.9}Se_{0.1}+xSnS_2$ exhibit large advantages over those of other SnS thermoelectrics (Fig. 2E) (*17, 47, 48, 51*), indicating the enlarged effective mass m^*. This comes

from the deepened Fermi level that is due to the higher hole carrier concentration in SnS after introducing SnS_2, which activates four valence bands that participated in carrier transport. To analyze the synergistic enhancement of m^* and μ, we further calculated the weighted mobility μ_w (Fig. 2F), which increases with the introduction of SnS_2, showing a similar trend to PF.

Promoting quadruple-band synglisis by introducing SnS_2

We investigated the crystal and electronic band structures associated with SR-XRD and DFT calculations. The detailed high-temperature SR-XRD patterns can be found in fig. S5. The diffraction peaks exhibited gradual shifts with rising temperatures, indicating dynamic lattice parameters owing to the distinctive continuous phase transition in SnS (*31*). The lattice parameters of *b* and *c* became closer at high temperatures, indicating the modified crystal symmetry. To quantitatively characterize the crystal symmetry evolution, we defined the angle θ between the Sn-Se bond and the
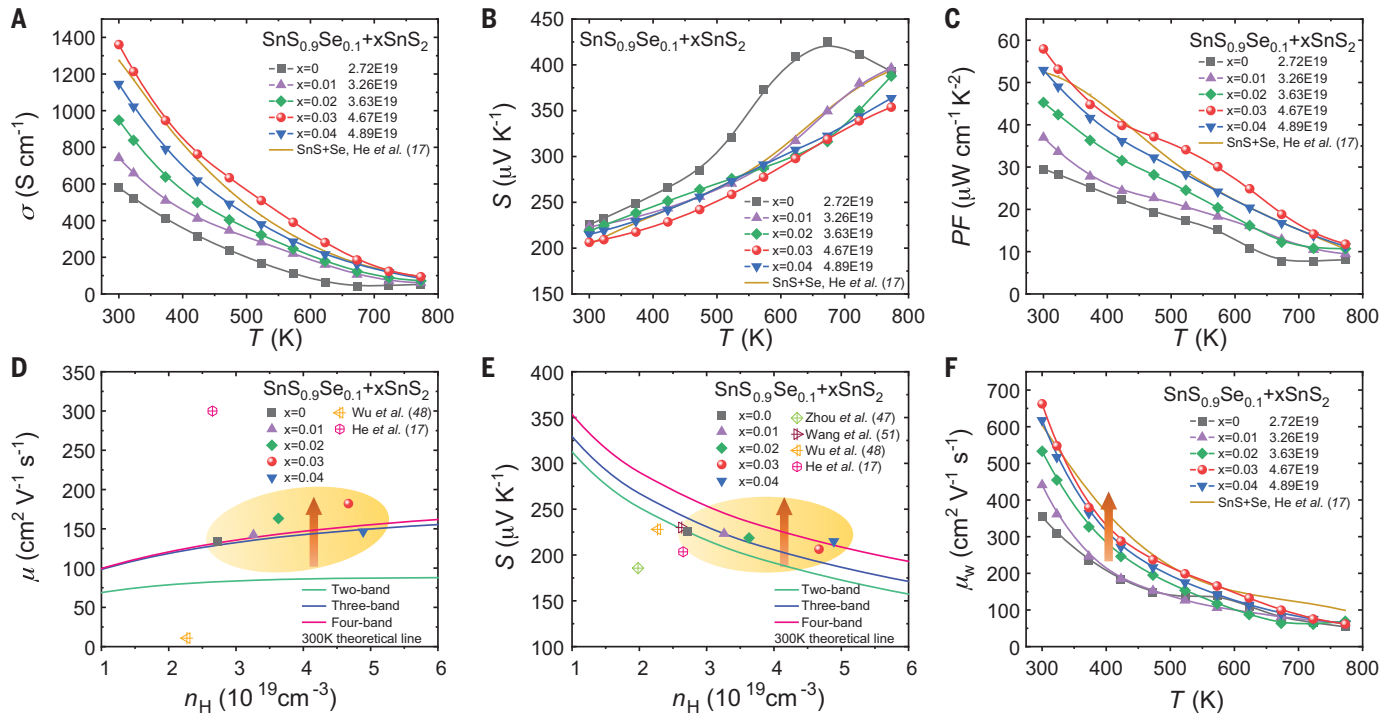
Fig. 2. Electrical transport properties of $SnS_{0.9}Se_{0.1}+xSnS_2$. (**A**) σ. (**B**) S. (**C**) PF. Comparison of (**D**) μ and (**E**) S as a function of n_H for $SnS_{0.9}Se_{0.1}+xSnS_2$ with that of other reported SnS thermoelectrics (*17, 47, 48, 51*) at room temperature. Theoretical lines for different band models are plotted. (**F**) Weighted mobility μ_w.
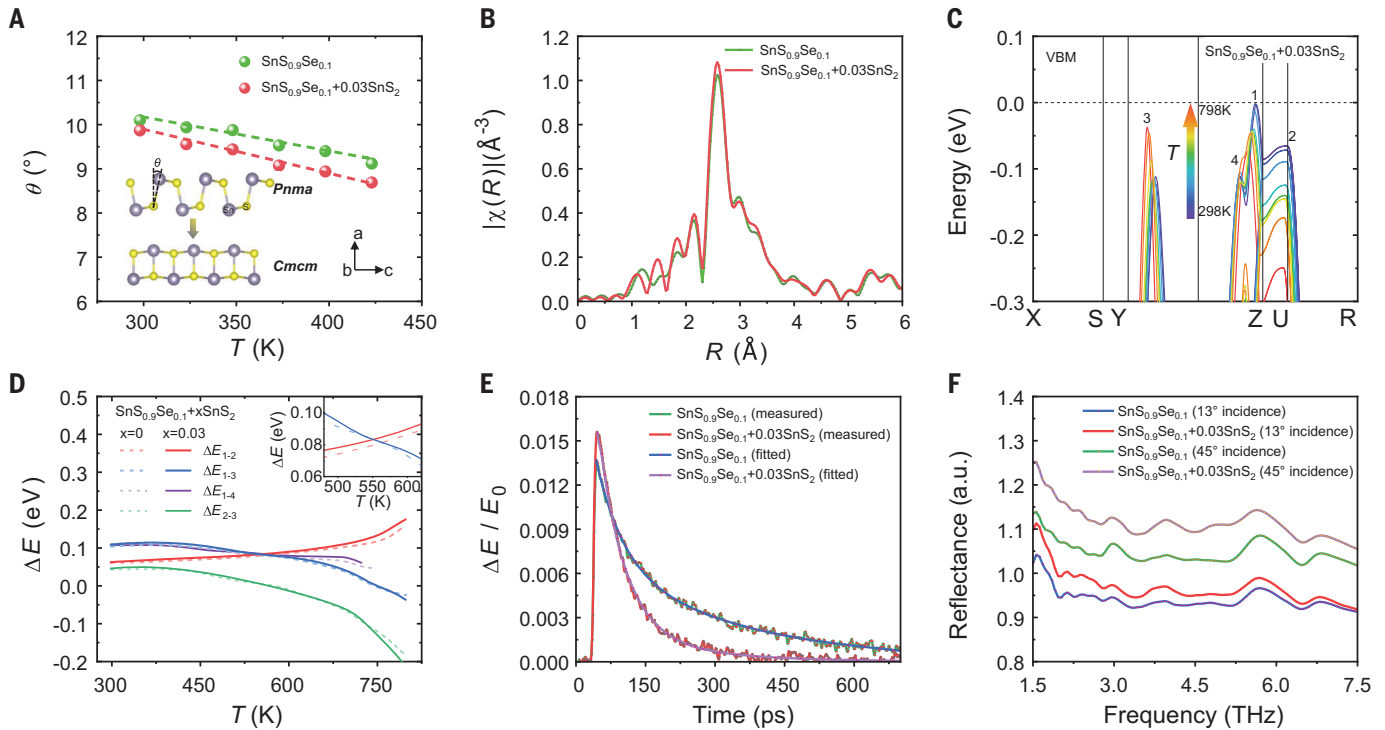

Fig. 3. The characterization of n and μ for $SnS_{0.9}Se_{0.1}+xSnS_2$ ($x = 0$ and 0.03) crystals by SR-XRD, XAFS, and THz spectroscopy measurements. (**A**) The temperature-dependent θ values in $SnS_{0.9}Se_{0.1}$ and $SnS_{0.9}Se_{0.1}+0.03SnS_2$, with the crystal structure schematically showing the definition of θ (lower θ values represent higher crystal symmetry). (**B**) The Fourier transform curves of Se K-edge $k^2\chi(k)$ oscillation functions (lower local disorder around Se atoms represents higher crystal symmetry). (**C**) Dynamic evolution of the four valence bands for $SnS_{0.9}Se_{0.1}+0.03SnS_2$. (**D**) Energy differences ΔE as a function of temperature between different VBM for $SnS_{0.9}Se_{0.1}$ and $SnS_{0.9}Se_{0.1}+0.03SnS_2$. The inset shows a magnified view. (**E**) Time-resolved THz spectroscopy measurements of $SnS_{0.9}Se_{0.1}+xSnS_2$ ($x = 0$ and 0.03) crystals in reflection mode. (**F**) Static THz reflection measurements under vacuum (a larger refractive index represents a higher carrier concentration n).

a-axis values as an indicator (lower θ values represent higher crystal symmetry). Precious temperature-dependent θ values (Fig. 3A) can be calculated by the atomic positions from the Rietveld refinements in tables S1 and S2. We obtained lower θ values in $SnS_{0.9}Se_{0.1}+0.03SnS_2$, indicating higher crystal symmetry, which facilitates the band synglisis of momentum (*27*). We also conducted x-ray absorption fine structure spectroscopy (XAFS) to evaluate the crystal symmetry. Our XAFS spectral analysis indicates an enhanced 2.6-Å coordination peak in R-space and a decreased local disorder around Se atoms in $SnS_{0.9}Se_{0.1}+0.03SnS_2$ (Fig. 3B, fig. S6, and table S3), confirming the enhanced crystal symmetry (*11, 27*). These crystal symmetry changes are expected to determine the evolution of electronic bands, thus modifying the electrical properties.

We conducted DFT calculations to investigate the temperature-dependent electronic band structures of $SnS_{0.9}Se_{0.1}$ and $SnS_{0.9}Se_{0.1}+0.03SnS_2$, using the atomic positions obtained from the SR-XRD data (figs. S7 and S8). The results show that the valence band difference between the two samples is consistent with the band structures of SnS with and without Sn vacancies based on the DFT calculations, indicating that Sn vacancy also plays a critical role in engineering the electronic band structure in SnS (fig. S9). The momentum and energy of VBM in $SnS_{0.9}Se_{0.1}$ and $SnS_{0.9}Se_{0.1}+0.03SnS_2$ transform substantially with rising temperatures (Fig. 3C, fig. S10, and movie S1). Specifically, the maximum energy difference between VBM1 and VBM4 (ΔE_{1-4}) is lowered to ~0.1 eV at 300 K for $SnS_{0.9}Se_{0.1}+0.03SnS_2$ and further gradually reduces with rising temperatures (Fig. 3D). VBM1 and VBM3 also progressively converge until realizing energy alignment, whereas VBM2 and VBM3 initially converge to energy alignment and then gradually diverge, exhibiting an overall crossover trend, consistent with observations in our previous work (*17*). Meanwhile, the pudding-mold bands (VBM 1 and VBM 4) merge into one band [VBM (1+4)] at 775 K, realizing the momentum alignment, which further facilitates carrier transport. The band structure differences between $SnS_{0.9}Se_{0.1}$ and $SnS_{0.9}Se_{0.1}+0.03SnS_2$ are mainly reflected in the following aspects (Fig. 1A). First, introducing SnS_2 lowers ΔE_{1-4}, facilitating the activation of VBM4 and realized four-band transport. Second, the momentum alignment temperature of VBM1 and VBM4 is reduced from ~775 K in $SnS_{0.9}Se_{0.1}$ to ~750 K in $SnS_{0.9}Se_{0.1}+0.03SnS_2$, activating bands synglisis at lower temperatures. Third, the energy alignment temperature of VBM2 and VBM3 is reduced from ~565 to ~550 K, which promotes convergence of the bands and thereby improves m^*. Collectively, the quadruple-band synglisis substantially facilitates carrier transport in $SnS_{0.9}Se_{0.1}+0.03SnS_2$,

leading to largely improved *PF* values across the entire temperature range (Fig. 1B).

To further investigate the difference in carrier transport between $SnS_{0.9}Se_{0.1}$ and $SnS_{0.9}Se_{0.1}+0.03SnS_2$, we conducted time-resolved THz spectroscopy measurements in reflection mode (Fig. 3E). The modulation of the reflected THz waves $\Delta E/E_0$ is traced by varying the time delay between the optical pump and the THz probe to explore μ. The fast decay constants we extracted are almost the same for $SnS_{0.9}Se_{0.1}$ and $SnS_{0.9}Se_{0.1}+0.03SnS_2$ (57.4 and 56.4 ps), whereas the slow decay constants differ markedly (300.3 and 195.2 ps), demonstrating the evidence of high carrier mobility even after introducing SnS_2 in $SnS_{0.9}Se_{0.1}$ (*52–54*). In addition, we conducted static THz reflection measurements under vacuum to elucidate the differences of carrier concentration *n* between two samples (Bruker 80v) (Fig. 3F). The re-

flection waves of $SnS_{0.9}Se_{0.1}+0.03SnS_2$ are higher than those of $SnS_{0.9}Se_{0.1}$ in both high-angle-incident and low-angle-incident modes, illustrating the improved refractive index *n*, which is consistent with the Hall measurements.

The increased n_H could be attributed to the formation of more Sn vacancies, which was also verified by using aberration-corrected scanning transmission electron microscopy (AC-STEM) to characterize the microstructure with and without introducing SnS_2. Fig. S11, A and B, shows the annular dark field STEM (ADF-STEM) images of $SnS_{0.9}Se_{0.1}$ and $SnS_{0.9}Se_{0.1}+0.03SnS_2$ along the [010] direction, respectively, where clusters of Sn vacancies are indicated by arrows. Results clearly illustrate that the density of Sn vacancies in $SnS_{0.9}Se_{0.1}+0.03SnS_2$ is significantly higher than that of $SnS_{0.9}Se_{0.1}$. Fig. S11, C and D, shows an enlarged region without and with Sn vacancies. The corresponding line profile of

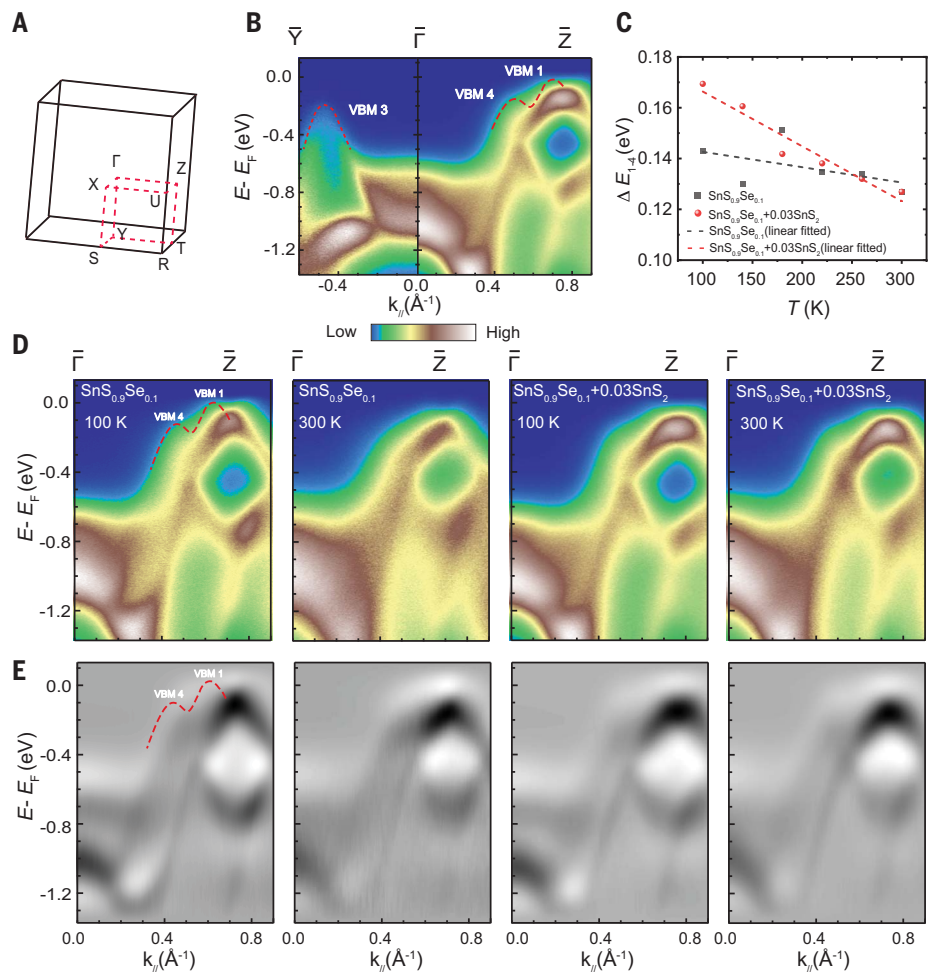**Fig. 4. Brillouin zone and band structures observed by ARPES.** (**A**) The Brillouin zone of SnS. (**B**) ARPES band structures of $SnS_{0.9}Se_{0.1}$ along the $\bar{Y} - \bar{\Gamma} - \bar{Z}$ direction. (**C**) The energy difference between VBM1 and VBM4 (ΔE_{1-4}) plotted as a temperature-dependent series, along with the results of linear fitting, which clearly shows the pronounced trend of band alignment with temperature after introducing SnS_2. (**D**) Electronic band structures for $SnS_{0.9}Se_{0.1}$ and $SnS_{0.9}Se_{0.1}+0.03SnS_2$ along the $\bar{\Gamma} - \bar{Z}$ plane at 100 and 300 K, respectively. (**E**) Second derivative plots corresponding to Fig. 4D. The red dashed line represents the theoretically calculated band structure.
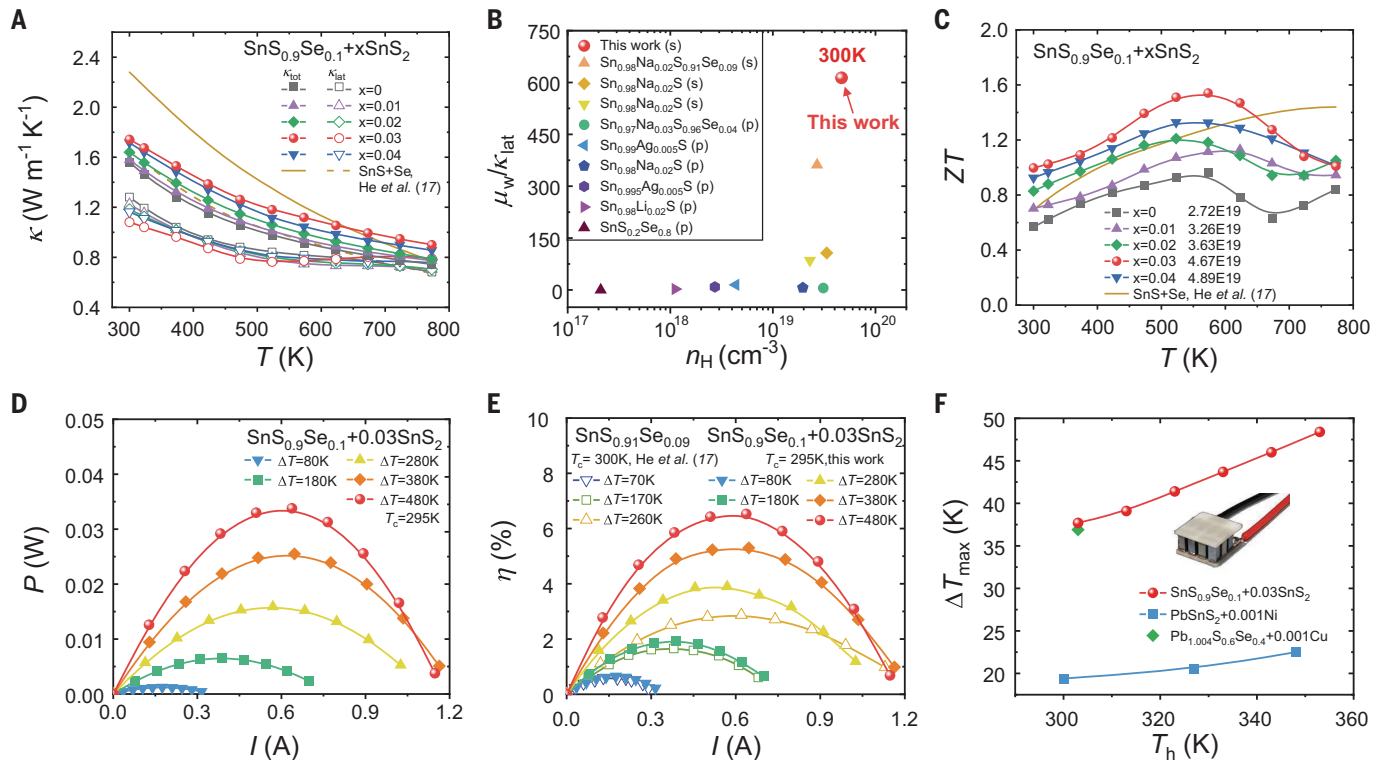
Fig. 5. κ, μ_w/κ_{lat}, ZT, and device performance for $SnS_{0.9}Se_{0.1}+xSnS_2$.
(**A**) κ_{tfot} and κ_{lat}. (**B**) Comparison of μ_w/κ_{lat} for $SnS_{0.9}Se_{0.1}+0.03SnS_2$ in this work with that of other reported SnS thermoelectrics (*17, 33, 47–49, 51, 57–59*). p, polycrystals; s, single crystals. (**C**) ZT values of $SnS_{0.9}Se_{0.1}+xSnS_2$. (**D**) Output power P and (**E**) power-generation efficiency η for the $SnS_{0.9}Se_{0.1}+0.03SnS_2$-based single-leg device. (**F**) Cooling ΔT_{max} for the seven-pair thermoelectric cooling device composed of p-type $SnS_{0.9}Se_{0.1}+0.03SnS_2$ crystals and n-type commercial $Bi_2Te_{2.7}Se_{0.3}$ as well as that for other reported sulfide-based thermoelectric devices (*66, 67*), with the inset figure showing the as-fabricated cooling device.

the boxed region in fig. S11E shows similar intensities at Sn peaks, whereas the line profiles in fig. S11F show decreased intensities at some Sn peaks, indicating the existence of Sn vacancies. Moreover, we conducted defect formation energy calculations for SnS in fig. S12. The formation energy of Sn vacancies in S-rich conditions is considerably lower than those of other point defects. This indicates that Sn vacancies are more stable and easier to form, consistent with the STEM results.

To directly observe the enhancement of quadruple-band synglisis induced by the introduction of SnS_2, we also investigated the evolution of the valence bands with various temperatures using ARPES (Fig. 4). The Brillouin zone for SnS is defined in Fig. 4A. Figure 4B displays the ARPES spectrum of $SnS_{0.9}Se_{0.1}$ along the $\bar{Y} - \Gamma - \bar{Z}$ direction. The ARPES spectrum shows that VBM3 is located along the $\Gamma - \bar{Y}$ direction, whereas VBM1 (which is located at the Fermi energy level $E_1 - E_F = 0$ eV) and VBM4 ($E_4 - E_F = -0.15$ eV) along the $\Gamma - \bar{Z}$ direction. The band arrangement for VBM1 and VBM4 form a pudding-mold band structure, which has been considered to be the origin of the excellent thermoelectric performance (*55, 56*). We measured the positions of VBM1 and VBM4 with temperature variations starting from

100 K and incrementing by 40 K up to 300 K and obtained the corresponding energy difference between them (ΔE_{1-4}) (Fig. 4C). The photoemission spectrum for both samples at the lowest temperature of 100 K and the highest temperature of 300 K are summarized in Fig. 4D, with data for other temperature points listed in fig. S13; Fig. 4E presents the corresponding second derivative plots for Fig. 4D.

Observing the temperature-induced relative shift of VBM1 and VBM4, we quantified the quadruple-band synglisis by calculating the energy difference ΔE_{1-4} between these VBM (the VBM1 and VBM4 peak positions are identified by Lorentzian fitting of the energy distribution curves). The relevant data, illustrated as a temperature-dependent series (Fig. 4C), elucidate their thermal evolution. Obviously, the ΔE_{1-4} of $SnS_{0.9}Se_{0.1}$ was approximately 0.143 eV at 100 K and gradually decreased with increasing temperature, reaching 0.127 eV at 300 K. After introducing SnS_2, the ΔE_{1-4} at 100 K increased to 0.17 eV compared with the original value. However, the effect of band alignment became more pronounced, and at ~260 K, the ΔE_{1-4} of the bands became closest in value, with both being 0.133 eV. Through linear fitting, after introducing SnS_2, the slope

of ΔE_{1-4} versus temperature changed from -6.03×10^{-5} to -2.15×10^{-4} eV K^{-1}, suggesting a substantial promotional effect of SnS_2 on multiple band transport, which is consistent with the DFT calculation results.

In addition to the evolution of VBM1 and VBM4 at the different temperatures mentioned above, we have also successfully pinpointed the locations of VBM1 and VBM3 by using the ARPES mapping. These positions serve as the basis for determining the direction of our measured dispersion, which cuts through both VBM 1 and VBM 3 (fig. S14, A and B). We measured the energy position change of VBM1 and VBM3 with increasing temperature for both $SnS_{0.9}Se_{0.1}$ and $SnS_{0.9}Se_{0.1}+0.03SnS_2$ and obtained the corresponding energy difference between them (ΔE_{1-3}), as shown in fig. S14, C to E. Through linear fitting analysis of the relative shift of VBM1 and VBM3, it was not difficult to find that after the introduction of SnS_2, the decline rate of ΔE_{1-3} with temperature became larger, indicating that SnS_2 has a substantial promotion effect on the quadruple-band synglisis, which is also consistent with the theoretical calculations. It is worth mentioning that after the introduction of SnS_2, the bandgap measured by optical diffuse reflection spectroscopy slightly decreased (fig. S15), which is also

consistent with the theoretical calculations and ARPES measurements.

ZT value, power generation, and Peltier cooling in devices

Aside from the improved electrical transport properties, the κ_{tot} of $SnS_{0.9}Se_{0.1}+0.03SnS_2$ remained low over the entire temperature range (Fig. 5A). $SnS_{0.9}Se_{0.1}+0.03SnS_2$ shows a higher κ_{tot} than $SnS_{0.9}Se_{0.1}$. κ_{tot} is composed of electronic (κ_{ele}) and lattice (κ_{lat}) parts (κ_{tot} = κ_{ele} + κ_{lat}). The thermal diffusivity (D), heat capacity (C_p), Lorentz number (L), κ_{ele}, and sample density (ρ) are shown in fig. S16 and table S4. The increased κ_{tot} is predominantly due to a higher κ_{ele}. Moreover, as the SnS_2 fraction increases, κ_{lat} is slightly reduced, which might be attributed to the strengthened phonon scattering by more Sn vacancies and possibly formed SnS_2 microdomains, similar to the observations in the $SnSe+SnSe_2$ system (50).

To investigate the distribution of SnS_2 in SnS, we further performed scanning electron microscopy (SEM) and AC-STEM characterizations on the pristine sample and the optimal $SnS+0.03SnS_2$ crystal. SEM images and energy dispersive spectrometer mappings at different scales show the uniform elemental distribution with no secondary phases in fig. S17. Fig. S18, A and B, shows the ADF-STEM images of $SnS_{0.9}Se_{0.1}$ and $SnS_{0.9}Se_{0.1}+0.03SnS_2$, respectively. SnS_2 is embedded in SnS matrix (fig. S18B), which is confirmed by its interlayer spacing, and the structure does not undergo phase separation over extended temperature cycling (fig. S19). Furthermore, the transition between SnS and SnS_2 layered structures was semicoherent, because the out-of-plane direction of SnS_2 aligns with SnS. Fig. S18, C and D, shows the fast Fourier transform power spectrum of the region in fig. S18, A and B, respectively, where planes corresponding to SnS and SnS_2 are marked. These observations indicate that SnS_2 is almost invisible in micrometer SEM images (fig. S17), and the distribution of each component element is uniform. However, in nanoscale ADF-STEM images, the addition of SnS_2 introduces more Sn vacancies as well as SnS_2 nanodomains, which effectively scatter phonons to lower the lattice thermal conductivity, and the semicoherent interface indicates that this microstructure does not adversely affect carrier transport.

We used μ_w/κ_{lat} and the quality factor B to evaluate the decoupling between electrical and thermal transport properties (Fig. 5B and fig. S20). The μ_w/κ_{lat} and B of $SnS_{0.9}Se_{0.1}+0.03SnS_2$ are substantially higher than those of the reported SnS thermoelectrics (17, 33, 47–49, 51, 57–59). As a result, the ZT value of $SnS_{0.9}Se_{0.1}+0.03SnS_2$ crystal reaches high value of ~1.0 at 300 K, nearly twice that of $SnS_{0.9}Se_{0.1}$ (Fig. 5C and fig. S21). Moreover, $SnS_{0.9}Se_{0.1}+0.03SnS_2$ shows ZT >1 across the entire measured temperature

range, especially at 300 to 623 K, resulting in a notable average ZT (ZT_{ave}) of ~1.3 at 300 to 773 K. Notably, the ZT_{ave} at 300 to 623 K for $SnS_{0.9}Se_{0.1}+0.03SnS_2$ surpasses that of most of the other sulfide-based thermoelectrics (fig. S22) (60–65).

Ultimately, we fabricated a single-leg thermoelectric device and used the commercial Mini-PEM instrument to characterize the power generation performance of $SnS_{0.9}Se_{0.1}+0.03SnS_2$ crystal (Fig. 5, D and E, and fig. S23). Specifically, we measured the voltage (V), output power (P), output heat flow (Q_{out}), and conversion efficiency (η) as a function of external current (I) with different temperature differences ΔT (the cold-end temperature T_c was fixed at ~295 K). P reaches a maximum value of ~0.035 W, and η reaches ~6.5% when ΔT is ~480 K, surpassing that of the reported p-type SnS crystals with triple-band convergence (17). Furthermore, we assembled a seven-pair thermoelectric cooling device using $SnS_{0.9}Se_{0.1}+0.03SnS_2$ crystals as p-legs and commercial $Bi_2Te_{2.7}Se_{0.3}$ as n-legs. With the hot-end temperature (T_h) fixed at ~303 K, this cooler achieves a maximum cooling temperature difference (ΔT_{max}) of ~37.7 K (Fig. 5F and fig. S24). Moreover, ΔT_{max} increases with rising T_h (fig. S24) and approaches ~48.4 K at T_h = 353 K, which is better than the reported sulfide-based thermoelectric coolers (66, 67).

The ΔT_{max} we obtained represents a sort of breakthrough for earth-abundant, wide-bandgap SnS-based thermoelectrics, in terms of developing a cooling device with high efficiency using this compound. However, we point out that the experimentally maximum η and ΔT_{max} values that we obtained are still lower than the theoretical values, which can be mainly attributed to several factors. First, the element sulfide in the SnS crystal easily reacts with most metals, resulting in a large contact resistance between the crystal and the conductive substrate. Through the combination of the phase diagrams and experimental trials (68), we expect to find a suitable interface material of SnS crystal with high reliability and low contact resistance. In addition, optimizing the geometry size of the cooler is expected to further increase the ΔT_{max}, which leaves room for future improvement.

Conclusions

We enhanced the thermoelectric properties of earth-abundant, wide-bandgap p-type SnS crystals by promoting the quadruple-band synglisis. The introduction of SnS_2 in SnS boosts the hole carrier concentration by forming more Sn vacancies and thus activates all four valence bands, substantially enhancing the electrical performance, whereas the Sn vacancy in SnS effectively favors the quadruple-band synglisis, enlarging the effective mass and resulting in high PF values over a broad temperature range, reaching ~58 $\mu W\ cm^{-1}\ K^{-2}$ at 300 K.

Ultimately, the substantially optimized electrical transport results in a ZT value of ~1.0 at room temperature and a high ZT_{ave} of ~1.3 at 300 to 773 K in the p-type $SnS_{0.9}Se_{0.1}+0.03SnS_2$ crystal. Our fabricated single-leg device generates a peak conversion efficiency of ~6.5% with a ΔT of ~480 K, and the cooling ΔT_{max} of the seven-pair cooler reaches ~37.7 and ~48.4 K when T_h is fixed at 303 and 353 K, respectively. The thermoelectric power generation and cooling performance of our $SnS_{0.9}Se_{0.1}+0.03SnS_2$ crystals are superior to those of other SnS-based thermoelectrics. Moreover, SnS offers substantial advantages, including earth abundance, low cost, and environmental friendliness, illustrating its substantial potential for widespread applications in thermoelectric power generation and cooling.

REFERENCES AND NOTES

1. Q. Yan, M. G. Kanatzidis, *Nat. Mater.* **21**, 503–513 (2022).
2. Z. Liu et al., *Mater. Lab* **1**, 220003 (2022).
3. G. Tan, L.-D. Zhao, M. G. Kanatzidis, *Chem. Rev.* **116**, 12123–12149 (2016).
4. S. Roychowdhury et al., *Science* **371**, 722–727 (2021).
5. B. Qin, L.-D. Zhao, *Mater. Lab* **1**, 220004 (2022).
6. Y. Xiao et al., *J. Am. Chem. Soc.* **142**, 4051–4060 (2020).
7. Y. Pei et al., *Nature* **473**, 66–69 (2011).
8. B. Jiang et al., *Science* **371**, 830–834 (2021).
9. Y. Jiang et al., *Nat. Commun.* **13**, 6087 (2022).
10. M. Zhang et al., *Adv. Funct. Mater.* **34**, 2307864 (2024).
11. D. Liu et al., *Science* **380**, 841–846 (2023).
12. J. Qiu et al., *Energy Environ. Sci.* **12**, 3106–3117 (2019).
13. W.-Y. Chen et al., *Chem. Eng. J.* **475**, 146428 (2023).
14. T. J. Slade et al., *Energy Environ. Sci.* **13**, 1509–1518 (2020).
15. J. Cai et al., *Adv. Energy Mater.* **12**, 2103287 (2022).
16. L.-D. Zhao et al., *Nature* **508**, 373–377 (2014).
17. W. He et al., *Science* **365**, 1418–1424 (2019).
18. C.-R. Guo, B.-C. Qin, D.-Y. Wang, L.-D. Zhao, *Rare Met.* **41**, 3803–3814 (2022).
19. X. Li et al., *Angew. Chem. Int. Ed.* **61**, e202212885 (2022).
20. W.-D. Liu, L. Yang, Z.-G. Chen, *Nano Today* **35**, 100938 (2020).
21. T. Xing et al., *Adv. Mater.* **33**, e2008773 (2021).
22. Y. Jin et al., *ACS Appl. Energy Mater.* **2**, 7594–7601 (2019).
23. Z. Liang et al., *Adv. Funct. Mater.* **33**, 2210016 (2023).
24. J. Mao et al., *Science* **365**, 495–498 (2019).
25. C. Chang, B. Qin, L. Su, L.-D. Zhao, *Sci. Bull.* **67**, 1105–1107 (2022).
26. L.-D. Zhao, C. Chang, G. Tan, M. G. Kanatzidis, *Energy Environ. Sci.* **9**, 3044–3060 (2016).
27. B. Qin et al., *Science* **373**, 556–561 (2021).
28. L. Su et al., *Science* **375**, 1385–1389 (2022).
29. C. W. Li et al., *Nat. Phys.* **11**, 1063–1069 (2015).
30. L.-D. Zhao et al., *Science* **351**, 141–144 (2016).
31. C. Chang et al., *Science* **360**, 778–783 (2018).
32. Q. Tan, J.-F. Li, *J. Electron. Mater.* **43**, 2435–2439 (2014).
33. Q. Tan et al., *J. Mater. Chem. A Mater. Energy Sustain.* **2**, 17302–17306 (2014).
34. M. Ibáñez et al., *Nat. Commun.* **7**, 10766 (2016).
35. L.-D. Zhao et al., *J. Am. Chem. Soc.* **134**, 16327–16336 (2012).
36. B. Jiang et al., *Energy Environ. Sci.* **13**, 579–591 (2020).
37. Z.-Z. Luo et al., *J. Am. Chem. Soc.* **144**, 7402–7413 (2022).
38. Y. He et al., *Adv. Mater.* **27**, 3639–3644 (2015).
39. K. Zhao et al., *Mater. Today Phys.* **1**, 14–23 (2017).
40. S. Zhao et al., *Mater. Today Phys.* **15**, 100271 (2020).
41. Y. Zhang et al., *Nano Energy* **85**, 105991 (2021).
42. C. Bourgès et al., *Acta Mater.* **97**, 180–190 (2015).
43. P. Zawadzki et al., *Appl. Phys. Lett.* **103**, 253902 (2013).
44. L. L. Baranowski et al., *Chem. Mater.* **26**, 4951–4959 (2014).
45. D. Weller, G. Kunkel, A. Ochs, D. Morelli, M. E. Anderson, *Mater. Today Phys.* **7**, 1–6 (2018).
46. R. Zhang, K. Chen, B. Du, M. J. Reece, *J. Mater. Chem. A Mater. Energy Sustain.* **5**, 5013–5019 (2017).

47. B. Zhou *et al.*, *ACS Appl. Mater. Interfaces* **9**, 34033–34041 (2017).
48. H. Wu *et al.*, *Adv. Energy Mater.* **8**, 1800087 (2018).
49. W. He *et al.*, *J. Mater. Chem. A Mater. Energy Sustain.* **6**, 10048–10056 (2018).
50. B. Qin *et al.*, *J. Am. Chem. Soc.* **142**, 5901–5909 (2020).
51. Z. Wang, D. Wang, Y. Qiu, J. He, L.-D. Zhao, *J. Alloys Compd.* **789**, 485–492 (2019).
52. J. Lou *et al.*, *Proc. Natl. Acad. Sci. U.S.A.* **119**, e2209218119 (2022).
53. Z. Jin *et al.*, *Light Sci. Appl.* **11**, 209 (2022).
54. Y. Lan *et al.*, *Sci. Adv.* **5**, eaaw5558 (2019).
55. H. Usui, K. Kuroki, *J. Appl. Phys.* **121**, 165101 (2017).
56. H. Usui *et al.*, *Phys. Rev. B* **88**, 075140 (2013).
57. B. Asfandiyar, B. Cai, L.-D. Zhao, J.-F. Li, *J. Materiomics* **6**, 77–85 (2020).
58. Y. Niu *et al.*, *IOP Conf. Ser. Mater. Sci. Eng.* **738**, 012016 (2020).
59. T.-R. Asfandiyar *et al.*, *Sci. Rep.* **7**, 43262 (2017).
60. F.-H. Sun *et al.*, *J. Materiomics* **10**, 218–233 (2024).
61. C. Bourgès *et al.*, *J. Am. Chem. Soc.* **140**, 2186–2195 (2018).
62. J. Guo *et al.*, *Adv. Funct. Mater.* **31**, 2102838 (2021).
63. M. Ohta, D. Y. Chung, M. Kunii, M. G. Kanatzidis, *J. Mater. Chem. A Mater. Energy Sustain.* **2**, 20048–20058 (2014).
64. G. Guélou *et al.*, *Chem. Mater.* **33**, 9425–9438 (2021).
65. T. Deng *et al.*, *Energy Environ. Sci.* **13**, 3041–3053 (2020).
66. S. Zhan *et al.*, *Adv. Funct. Mater.* **34**, 2406428 (2024).
67. L. Wang *et al.*, *Nat. Commun.* **15**, 3782 (2024).
68. L. Xie *et al.*, *Science* **382**, 921–928 (2023).

ACKNOWLEDGMENTS

SUPPLEMENTARY MATERIALS